

Locating and modeling regional earthquakes with two stations

Ying Tan,¹ Lupei Zhu,² Donald V. Helmberger,¹ and Chandan K. Saikia³

Received 11 April 2005; revised 3 October 2005; accepted 31 October 2005; published 31 January 2006.

[1] We developed a new technique CAPloc to retrieve full source parameters of small seismic events from regional seismograms, which include origin time, epicenter location, depth, focal mechanism, and moment magnitude. Despite rather complicated propagation effects at short periods, a simple localized one-dimensional model can well explain signals of periods 3–10 s if we break the three-component records into different segments and allow differential time shifts among them. These differential time shifts, once established from a calibration process or a well-determined tomographic map, can be used together with *P* wave travel times to refine an event's location. In this study, we tested whether our new method could produce satisfactory results with as few as two stations, so that we can improve source estimates of poorly monitored events with sparse waveform data. We conducted the test on 28 events in the Tibetan Plateau. The focal mechanisms and locations determined from only two stations agree well with those determined from a whole PASSCAL array. In particular, our new method produces better locations than International Seismological Centre, with the average mislocation error reduced from ~ 16 to ~ 5 km. We also tested whether an event's depth and mechanism can be determined separately from its epicenter relocation in a two-step approach. We find that the two-step approach does not always give the correct solution, but the reliability of a solution can be evaluated using a reduced chi-square value.

Citation: Tan, Y., L. Zhu, D. V. Helmberger, and C. K. Saikia (2006), Locating and modeling regional earthquakes with two stations, *J. Geophys. Res.*, 111, B01306, doi:10.1029/2005JB003775.

1. Introduction

[2] Rapid characterization of a seismically recorded event has been one of the major themes of seismic monitoring. An efficient and accurate way to retrieve the hypocenter, mechanism, origin time and size of a seismic event is important for understanding tectonic processes, responding to earthquake hazards, as well as discriminating nuclear explosions from natural earthquakes.

[3] Classic methods assume a good seismic velocity model and use travel times of certain seismic phases, usually the direct *P* and/or *S* wave, to locate an event's hypocenter, and phase polarities for determining the focal mechanism. Consequently, the accuracy of the solutions depends on the station coverage, since most velocity models used are good only for a global average. In that sense, large events with magnitude greater than ~ 5.5 , that are readily recorded globally, are usually well determined. However, a much larger population of smaller events, where only limited regional data ($\Delta < 10^\circ$) have adequate signal-to-noise ratio (SNR), are more prone to biases caused by structural heterogeneity.

[4] A reinforced regional seismic network allows enough redundancy to average out some of the local complications. The implementation of TriNet with over 150 broadband stations in southern California is such an example, where an event's origin time, hypocenter, mechanism and size are well determined and reported on the Web within minutes [Hauksson, 2001]. Similar real-time systems have been developed in recent years in other seismically active regions to monitor seismic activity for rapid notification and damage assessment [e.g., Teng *et al.*, 1997; Okada *et al.*, 2004]. In addition, temporarily deployed dense local seismic networks have provided rare opportunities to retrieve reliable regional source parameters in some geologically interesting, but remote areas [e.g., Leitner *et al.*, 2001; Langin *et al.*, 2003]. However, although these well-determined regional events prove useful to constrain the thermal structure and understand the active tectonics, a substantial increase in their number is needed to further explore spatial and temporal variations. Therefore a reliable method is needed to extract accurate source parameters from sparse recordings of poorly monitored events. These could be historical events that occurred before the modern era of dense instrumentation in southern California, or those in some remote areas, such as southeastern Asia or the Middle East. Our method will also support the verification of the Comprehensive Nuclear Test Ban Treaty (CTBT), which requires accurate location determination of global seismicity with a fixed teleseismic network [Kennett and Ringdal, 2001].

¹Seismological Laboratory, California Institute of Technology, Pasadena, California, USA.

²Department of Earth and Atmospheric Sciences, Saint Louis University, St. Louis, Missouri, USA.

³URS Co., Pasadena, California, USA.

[5] Better utilizing a limited data set becomes the major concern in developing such a method. Efforts are basically divided into two categories, focusing on accurate source location and focal mechanism, respectively. Tremendous work has been done to better locate a seismic event in the context of the CTBT. Various strategies include developing new techniques for more accurate travel time measurements, utilizing travel times together with slowness and azimuth information [e.g., Bondár and North, 1999; Bondár et al., 1999; Uhrhammer et al., 2001], implementing better regional velocity models [e.g., Kremenetskaya et al., 2001], and deriving various source-specific station corrections [e.g., Yang et al., 2001a, 2001b; Ryaboy et al., 2001]. At the same time, rather than focusing on travel times of impulsive body wave phases, Yacoub [1996] reported locations of 16 nuclear explosions that were well determined by using arrival times of the maximum Rayleigh wave energy estimated over a narrow frequency band of 17–23 s, in the same manner as P wave travel times are used. Similar experiments and results were reported later by Stevens et al. [2001]. The improvement on epicenter location from various validation tests is encouraging. Accurate depth determination is, however, still an open issue.

[6] On the other hand, modeling regional seismograms provides the only opportunity to constrain an event's source mechanism accurately when a reliable first motion focal plot cannot be constructed. Early work by Langston [1981] showed that the relative amplitudes of P , SH and SV waveforms from a World Wide Standardized Seismograph Network (WWSSN) station are sufficient to discriminate between fault types. With the development of modern broadband seismic instrumentation and the success in modeling broadband records, Dreger and Helmberger [1993] demonstrated the feasibility of retrieving stable source orientations using long-period body waves (mainly Pnl and S_n) from a couple of early southern California broadband stations. Their work paralleled that of Fan and Wallace [1991] in New Mexico. Surface waves also prove useful in source mechanism determination as demonstrated by several authors addressing different periods (10–50 s [Thio and Kanamori, 1995], 15–50 s [Romanowicz et al., 1993], and >50 s [Ritsema and Lay, 1993]). However, the methods using surface waves alone require some azimuthal sampling around the source, which makes them less effective in cases, where only a few stations are available. A step forward in using both body and surface waves was made in the so called “cut and paste” method (CAP) [Zhao and Helmberger, 1994; Zhu and Helmberger, 1996], where body wave and surface waves from entire records are separated and modeled with differential time shifts between them allowed. This method desensitizes the timing between the principal crustal arrivals, hence accurate source estimates could be achieved with imperfect Green's functions.

[7] Here based on an expansion of the CAP method, we present a joint effort to determine both event locations and focal mechanisms using complete three-component regional seismograms. We call the new method CAPloc to distinguish it from the original CAP. The basis of the method lies in that, as the waveforms of major seismic arrivals constrain an event's source depth and orientation, their differential travel times confine the epicenter location. To put the method into practice requires calibration of the regional

paths. In their study, Zhu et al. [2006] have conducted an effective calibration process with a temporary PASSCAL array on the Tibetan Plateau, where we will validate our method by demonstrating its ability to recover essentially the same source parameters derived from a well distributed array with only two fixed stations.

2. Methodology

[8] Let $u(t)$ be a recorded seismogram with instrument response removed. The corresponding synthetics $s(t)$ for a double couple source can be expressed as a summation of contributions from three fundamental faults, namely, vertical strike slip, vertical dip slip and 45° dip slip:

$$s_j(t) = M_0 \sum_{i=1}^3 A_{ij}(\phi - \varphi(\theta, \xi), \delta, \lambda) G_{ij}(h, \Delta(\theta, \xi), t), \quad (1)$$

where $j = 1, 2, 3$ denote the vertical, radial, and tangential components, respectively [Helmberger, 1983]. The G_{ij} 's are the Green's functions, and the A_{ij} 's are the radiation coefficients. M_0 is the scalar moment. φ and Δ are the station azimuth and distance. The unknowns, h (depth), ϕ (strike), δ (dip) and λ (rake), that describe the source depth and orientation, together with θ (event latitude) and ξ (event longitude), that define the epicenter location, can be obtained by solving the equation

$$u(t) = s(t). \quad (2)$$

Since there are only limited unknowns and all of them are confined within a certain range of values, it is straightforward and convenient to solve the equation in a grid search manner.

[9] However, solving equation (2) with an entire regional record is problematic. First, regional records are usually complicated by three-dimensional (3-D) path and site effects. In particular, different portions of the records, e.g., the body wave (Pnl) and surface waves, which sample different parts of the crust, require different adjustments on the 1-D Green's functions over different frequency bands. Secondly, whole waveform inversion is easily dominated by the strongest signals, usually the surface waves. To overcome these difficulties, we expand the original CAP source estimation technique [Zhao and Helmberger, 1994; Zhu and Helmberger, 1996], which breaks an entire record into Pnl and surface wave segments to be modeled separately.

[10] We use the chi-square χ_w^2 as our object function:

$$\chi_w^2 = \frac{e_{Pnl}^2}{\sigma_{Pnl}^2} + \frac{e_{Sur}^2}{\sigma_{Sur}^2}, \quad (3)$$

where the waveform misfit errors

$$e_{Pnl} = \|u^{Pnl}(t) - s^{Pnl}(t - \Delta T)\| \quad (4)$$

$$e_{Sur} = \|u^{\text{Rayleigh}}(t) - s^{\text{Rayleigh}}(t - \Delta T - \delta t^{\text{Rayleigh}})\| + \|u^{\text{Love}}(t) - s^{\text{Love}}(t - \Delta T - \delta t^{\text{Love}})\|. \quad (5)$$

Here parallels denote the L_2 norm. ΔT is the time shift to align synthetics with data on the first P arrival. The $\delta t^{\text{Rayleigh}}$ and δt^{Love} are the path specific timing corrections for the synthetic Rayleigh and Love wave segments with respect to the first P arrival, which can be derived from a simple calibration process as discussed by *Zhu et al.* [2006] or using a well-determined tomographic map. These δt account for the deviations of real crustal structure from the 1-D model. They are prerequisite for an accurate epicenter relocation. If we set them as free parameters to be determined by waveform cross correlation in the grid search, the source depth and orientation can still be determined but not the epicenter location, since the mislocation errors are absorbed by these time shifts.

[11] The parameters σ_{Pnl}^2 and σ_{Sur}^2 in equation (3) are the variances of waveform residuals of Pnl and surface waves. They measure how well the velocity model can explain the observed waveforms. We distinguish Pnl and surface waves, because they sample the velocity structure differently. Since σ_{Pnl}^2 and σ_{Sur}^2 are usually not known a priori, we conduct a series of trial grid searches with a range of $\sigma_{\text{Sur}}/\sigma_{Pnl}$ ratios to minimize

$$\chi_w'^2 = \sigma_{\text{Sur}}^2 \chi_w^2 = \frac{\sigma_{\text{Sur}}^2}{\sigma_{Pnl}^2} e_{Pnl} + e_{\text{Sur}}. \quad (6)$$

The best $\sigma_{\text{Sur}}/\sigma_{Pnl}$ ratio is selected when the misfit errors of Pnl and surface waves are “equal”:

$$\frac{1}{\nu_{\text{Sur}}} \frac{e_{\text{Sur}}}{\sigma_{\text{Sur}}^2} = \frac{1}{\nu_{Pnl}} \frac{e_{Pnl}}{\sigma_{Pnl}^2}. \quad (7)$$

Here, ν_{Pnl} and ν_{Sur} are the numbers of measurements from Pnl and surface wave waveform data, respectively. Since an individual data point on a seismogram strongly correlates with its neighbors, we count every duration of the dominant period as one independent “data point”.

[12] By using equation (7) and equation (4.26) of *Bevington and Robinson* [2003], σ_{Pnl}^2 and σ_{Sur}^2 can then be estimated a posteriori from the misfit errors of Pnl and surface waves at the best solution:

$$\sigma_{Pnl}^2 = \frac{\nu_{Pnl} + \nu_{\text{Sur}}}{\nu_{Pnl} + \nu_{\text{Sur}} - m} \frac{e_{Pnl}}{\nu_{Pnl}}, \quad (8)$$

$$\sigma_{\text{Sur}}^2 = \frac{\nu_{Pnl} + \nu_{\text{Sur}}}{\nu_{Pnl} + \nu_{\text{Sur}} - m} \frac{e_{\text{Sur}}}{\nu_{\text{Sur}}}, \quad (9)$$

where m is the number of unknown source parameters.

[13] Thus the relative weight between Pnl and surface waves in our new CAPloc is adaptive as compared to a fixed value in the original CAP [*Zhu and Helmberger*, 1996]. Later we will show that a static weighting factor of Pnl to surface waves is not appropriate, especially when few stations are used.

[14] We can place an additional constraint on the event location by minimizing P wave traveltime residuals

$$\chi_t^2 = \frac{1}{\sigma_t^2} \sum_{n=1}^N \left(\Delta T_n - \frac{1}{N} \sum_{n=1}^N \Delta T_n \right)^2, \quad (10)$$

where σ_t^2 represents the variance of the residuals. Provided that structural effects on these travel time residuals can be corrected by a path calibration or tomographic study, σ_t^2 mainly measures uncertainty in picking P wave arrivals. The average of the traveltime residuals, $\frac{1}{N} \sum_{n=1}^N \Delta T_n$, implies an offset in the event’s origin time.

[15] We simply search through the whole parameter space of all the unknowns h , ϕ , δ , λ , θ and ξ , and determine the best solution of the source parameters where

$$\chi^2 = \chi_w^2 + \chi_t^2 \quad (11)$$

is minimized. However, since the waveforms of Pnl and surface waves are mainly controlled by source depth and orientation, while their travel times only depend on event location, we can also separate the whole parameter space into two subspaces of $(h, \phi, \delta, \lambda)$ and (θ, ξ) , and conduct two grid searches separately on them. The first one is to determine source depth and orientation with an event’s preliminary epicenter location by minimizing χ_w^2 , where $\delta t^{\text{Rayleigh}}$ and δt^{Love} are set as free parameters determined by waveform cross correlation to account for both event mislocation and structural effect. Then, using the obtained source depth and mechanism, a second grid search is conducted for a better epicenter location, where the surface wave segments are no longer allowed to float, but fixed with predetermined time shifts from either path calibration or seismic tomography. Compared to the one-step approach, this two-step approach has the advantage of requiring less computation time. However, as it might be predicted, a wrong source depth or mechanism from the first step could lead to a wrong relocation. In section 3, we will test both approaches.

3. Applications

3.1. Data

[16] The Tibetan Plateau was chosen as our test bed mainly based on two considerations. First, Tibet itself is a seismically active, but poorly monitored region with a sparse short-period network plus a couple of modern broadband instruments. Second, *Zhu et al.* [2006] have obtained useful calibration information for various regional paths on the plateau using data collected by a temporary PASSCAL experiment in 1991–1992 [*Owens et al.*, 1993]. Moreover, the events they have studied with locations, depths, and mechanisms well determined from the whole PASSCAL array are ideal for testing the validity of our new method. Figure 1 displays locations of over 50 earthquakes investigated by *Zhu et al.* (submitted manuscript, 2005). The average relocation offset with respect to the ISC locations is ~ 16 km, excluding the two events mislocated by ISC by over hundreds of kilometers. The offsets generally correlate well with the ISC station coverage: smaller offsets are associated with better coverage.

[17] To test our method, we choose two fixed stations, LHASA and TUNL, and the 28 events that were recorded by both. The two stations were separated by over five hundred kilometers, so they provide nearly independent constraints for all of the selected events. Furthermore, they are the sites of two permanent broadband seismic

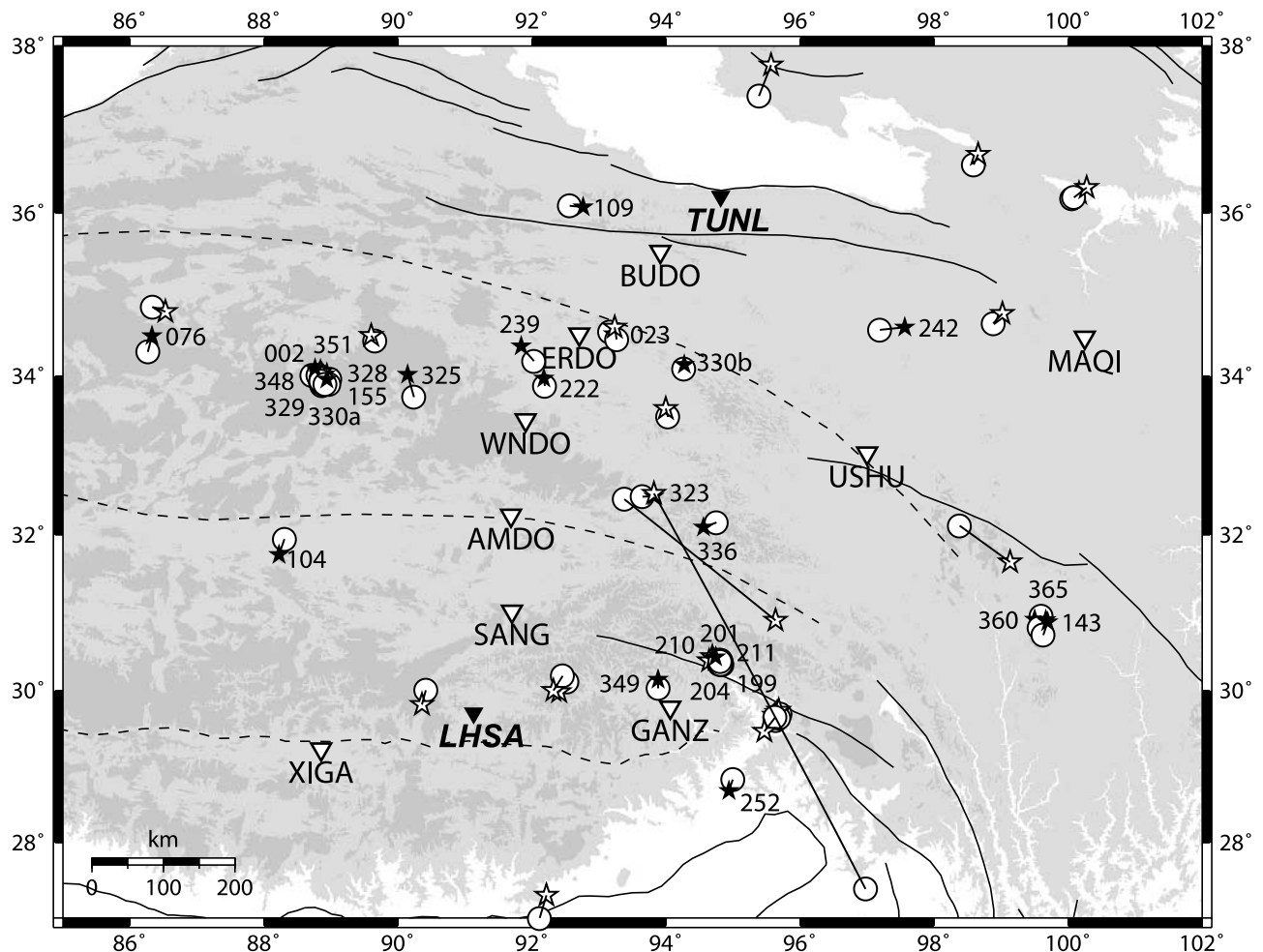


Figure 1. Temporary stations (inverse triangles) of the 1991–1992 PASSCAL experiment on the Tibetan Plateau with 53 recorded earthquakes. The circles represent the events' ISC locations, and the stars represent their relocations using the full array by *Zhu et al.* [2006]. The solid stars indicate the 28 events selected in this study, which were recorded by both stations LHASA and TUNL (solid triangles). Labels are their Julian day numbers.

stations in Tibet. Therefore our study will benefit future earthquake source determination in the region. Using the same two stations for all the events can avoid possible biases in data selection and ensure a fair assessment of our method.

[18] Three-component seismograms of an event 330b located between the two stations are displayed in Figure 2 as an example. The data are shown in different frequency bands. Note that one advantage of having broadband waveform data is that several crustal phases can be well recognized when the waveforms are examined in different frequency bands. For example, while the long-period *Pnl* waves are weak, the short-period *P* waves are strong and useful for picking *P* wave arrival times and polarities. Different bandpass filters, 3–20 s for *Pnl* and 10–50 s for surface waves, are chosen mainly based on previous waveform modeling results. For example, *Zhu and Helmberger* [1996] found that allowing short-period energy (~ 3 –20 s) into the *Pnl* window helps resolve the depth phases. Surface waves at short periods are heavily influenced by shallow crustal structures, but they are stable over a lower frequency band of 10–50 s [see also *Ritsema and Lay*, 1993]. Although

we have examined other frequency ranges, the filters applied on the records shown in Figure 2 proved optimal and thus were used throughout this study.

[19] In the following, we will apply the two approaches of our method to the selected 28 events using the two stations and compare the results with those determined from the whole PASSCAL array [*Zhu et al.*, 2006]. We use the same 1-D Tibetan velocity model (T93) by *Zhu et al.* [2006] to facilitate the use of path calibration they developed. The Green's functions are computed using a reflectivity code [*Zhu and Rivera*, 2002] with a 5 km interval in both depth and distance.

3.2. The One-Step Approach

[20] We first test the one-step approach, where the source depth, mechanism and epicenter location are simultaneously determined in one grid search. The target parameter space of strike, dip, rake and depth is chosen as 0 – 360° , 0 – 90° , -90 – 90° , and 0 – 40 km, respectively. For each event, we search the epicentral area of a $1^\circ \times 1^\circ$ square surrounding its ISC location. A searching step of 10° is used for the fault parameters, 5 km for the depth and 0.05° for both the

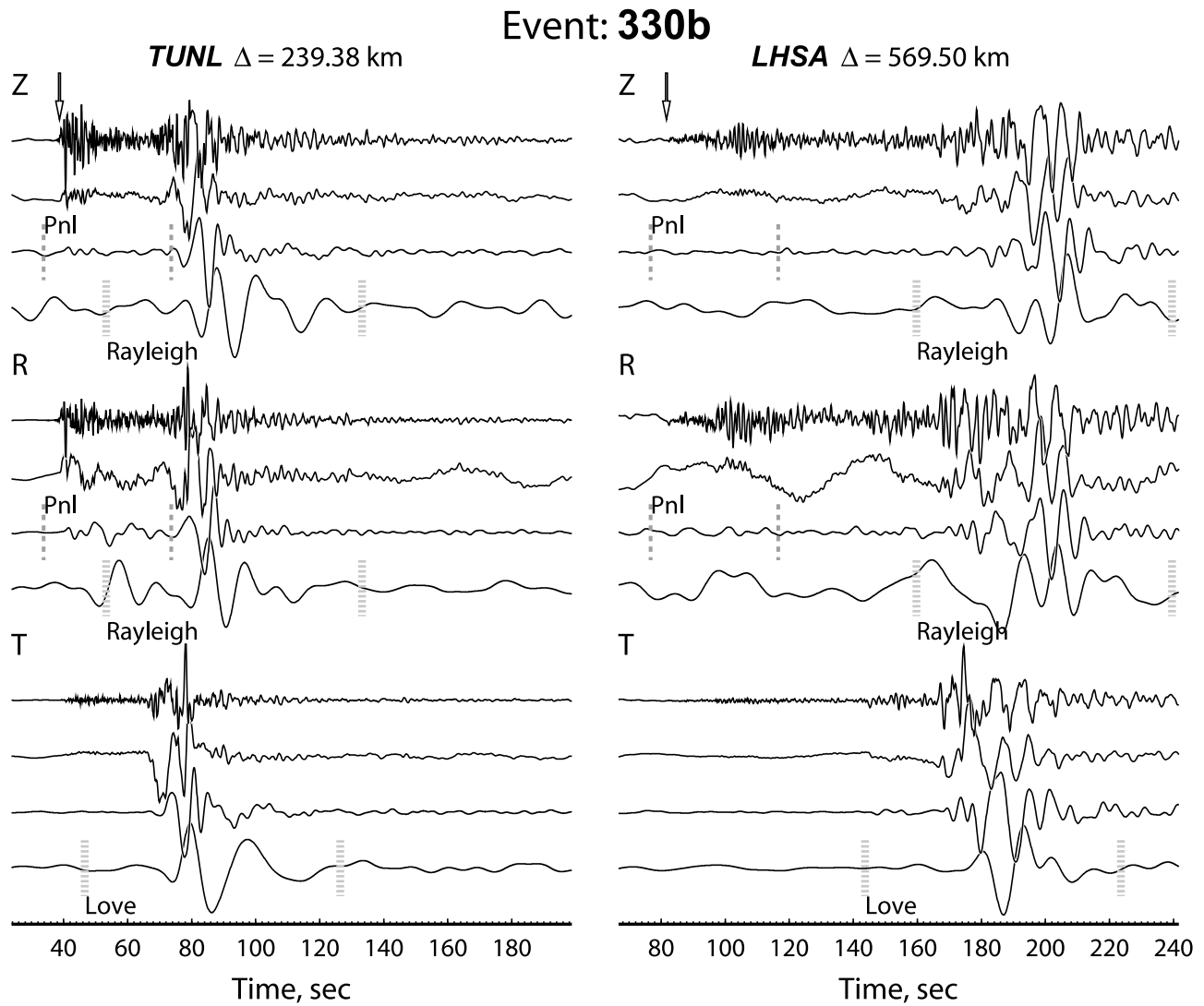


Figure 2. Three-component records from event 330b at the two stations (left) TUNL and (right) LHSA in different frequency bands. The top trace of each component displays the broadband velocity record with an arrow on the vertical (Z) component indicating the onset of *P* wave. The following traces are the integrated displacements without filtering and with band-pass filters, 0.05–0.3 Hz and 0.02–0.1 Hz. The time windows of the *Pnl* and surface waves are determined by the epicentral distance using apparent velocities of *P* (6.5 km/s), *S* (3.8 km/s), Rayleigh (3.1 km/s), and Love (3.4 km/s) waves, as indicated by the dashed lines.

latitude and longitude since our Green's functions are computed with a 5 km interval. The time shifts of Rayleigh and Love waves, i.e., $\delta t^{\text{Rayleigh}}$ and δt^{Love} , are fixed to the corresponding empirical-path-specific corrections (EPSCs) established by the relocated events [Zhu *et al.*, 2006]. However, to account for the discreteness of the finite grid size, we allow the δt 's to vary within ± 0.5 s of the assigned values, as determined by waveform cross correlation during the grid search. This is equivalent to assuming a 0.5 s uncertainty in the calibration result.

[21] The whole procedure is illustrated in Figures 3 and 4 with two events 222 and 104 as examples. We try a range of $\sigma_{\text{Sur}}/\sigma_{\text{Pnl}}$ ratios from 0.0 to 10.0 in the grid searches to minimize χ_w^2 in equation (6), and the best $\sigma_{\text{Sur}}/\sigma_{\text{Pnl}}$ ratio is selected when equation (7) is satisfied. Quite different $\sigma_{\text{Sur}}/\sigma_{\text{Pnl}}$ ratios, 1.6 for event 222 and 7.6 for event 104,

are obtained as shown in Figures 3 and 4. The solutions of source parameters in the vicinity of the best $\sigma_{\text{Sur}}/\sigma_{\text{Pnl}}$ ratio appear rather stable. However, different depths, mechanisms, and epicentral locations are produced when the $\sigma_{\text{Sur}}/\sigma_{\text{Pnl}}$ ratio departs significantly from the best value. Consequently, the resulted waveform fits change. For event 222 (Figure 3), as a $\sigma_{\text{Sur}}/\sigma_{\text{Pnl}}$ ratio of 4.0 over weights the *Pnl* waves, a shallower source of ~ 5 km deep and north-westward by ~ 15 km is produced compared to that with the best $\sigma_{\text{Sur}}/\sigma_{\text{Pnl}}$ ratio (1.6). Although the *Pnl* waves are slightly better fitted, the larger $\sigma_{\text{Sur}}/\sigma_{\text{Pnl}}$ ratio reduces the weight on the surface waves and causes apparently poorer Rayleigh wave waveform fits. Event 104 (Figure 4) requires a much larger $\sigma_{\text{Sur}}/\sigma_{\text{Pnl}}$ ratio of 7.6. A small $\sigma_{\text{Sur}}/\sigma_{\text{Pnl}}$ ratio, such as 2.0, leads to a deeper source and a slightly changed mechanism. Though the waveform fits of surface waves

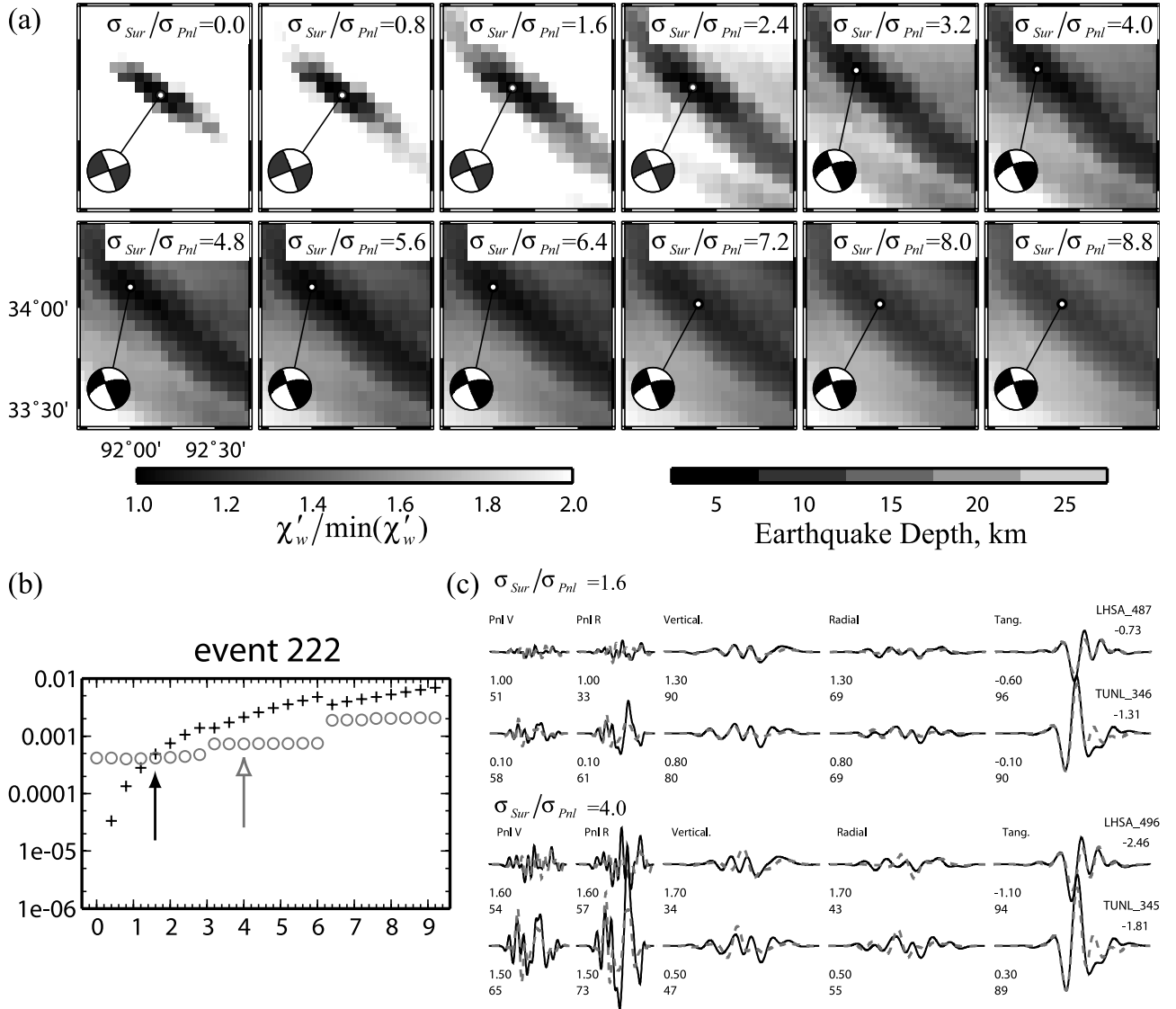


Figure 3. One-step grid search results for event 222. (a) Best solutions of source parameters with different $\sigma_{Sur}/\sigma_{Pnl}$ ratios. (b) Waveform misfit error as a function of $\sigma_{Sur}/\sigma_{Pnl}$ ratio. The crosses and circles display $(\sigma_{Sur}^2)(\sigma_{Pnl}^2)/(\nu_{Sur})(\nu_{Pnl}) e_{Pnl}$ and e_{Sur} , respectively. The best $\sigma_{Sur}/\sigma_{Pnl}$ ratio is chosen when the two are equal (indicated by the black arrow) (c) (top) Waveform fits from the solution with the best $\sigma_{Sur}/\sigma_{Pnl}$ ratio (1.6) and (bottom) those from the solution with a different $\sigma_{Sur}/\sigma_{Pnl}$ ratio of 4.0. The *Pnl* waves are plotted with the scaling factor of $\sigma_{Sur}/\sigma_{Pnl}$. The numbers below the traces are the differential time shifts in seconds determined by cross correlation (cc) and the corresponding cc coefficients.

remain similar, the larger $\sigma_{Sur}/\sigma_{Pnl}$ ratio puts more weight on the *Pnl* waves and subsequently improves the *Pnl* waveform fit at station LHS4, where the cross-correlation coefficients between the observed and synthetic *Pnl* waves are increased from 22/38 to 71/78 (Figure 4). This underlines the importance of the adaptive weighting scheme between *Pnl* and surface waves in our CAPloc method. Since *Pnl* and surface waves provide nearly independent constraint in source characterization, and their amplitude ratio is a useful depth indicator, using both *Pnl* and surface waves is more effective and desired, particularly when few stations are used. An inappropriate relative weight between *Pnl* and surface waves, such as the static *Pnl* weight used in the original CAP by Zhu and Helmberger [1996], can easily cause an

imbalance between the two, thus losing the constraint from the weaker component as shown in both Figures 3 and 4. The large variation in $\sigma_{Sur}/\sigma_{Pnl}$ ratios obtained for different events (see Table 1) is mainly due to the rather limited azimuthal coverage of the two stations.

[22] We estimate the variances σ_{Pnl}^2 and σ_{Sur}^2 using the best $\sigma_{Sur}/\sigma_{Pnl}$ ratio from equation (8) and (9). Then we add in the *P* wave travel time constraint (equation (10)) to find the best solution of source depth, mechanism and epicenter location that minimizes χ^2 in equation (11). A σ_t^2 value of 0.09 s^2 is used by assuming an uncertainty of 0.3 s in reading *P* wave arrival times. The results for all the 28 events are summarized in Table 1, and the details of 20 events are displayed in Figure 5, where we choose two events from each event

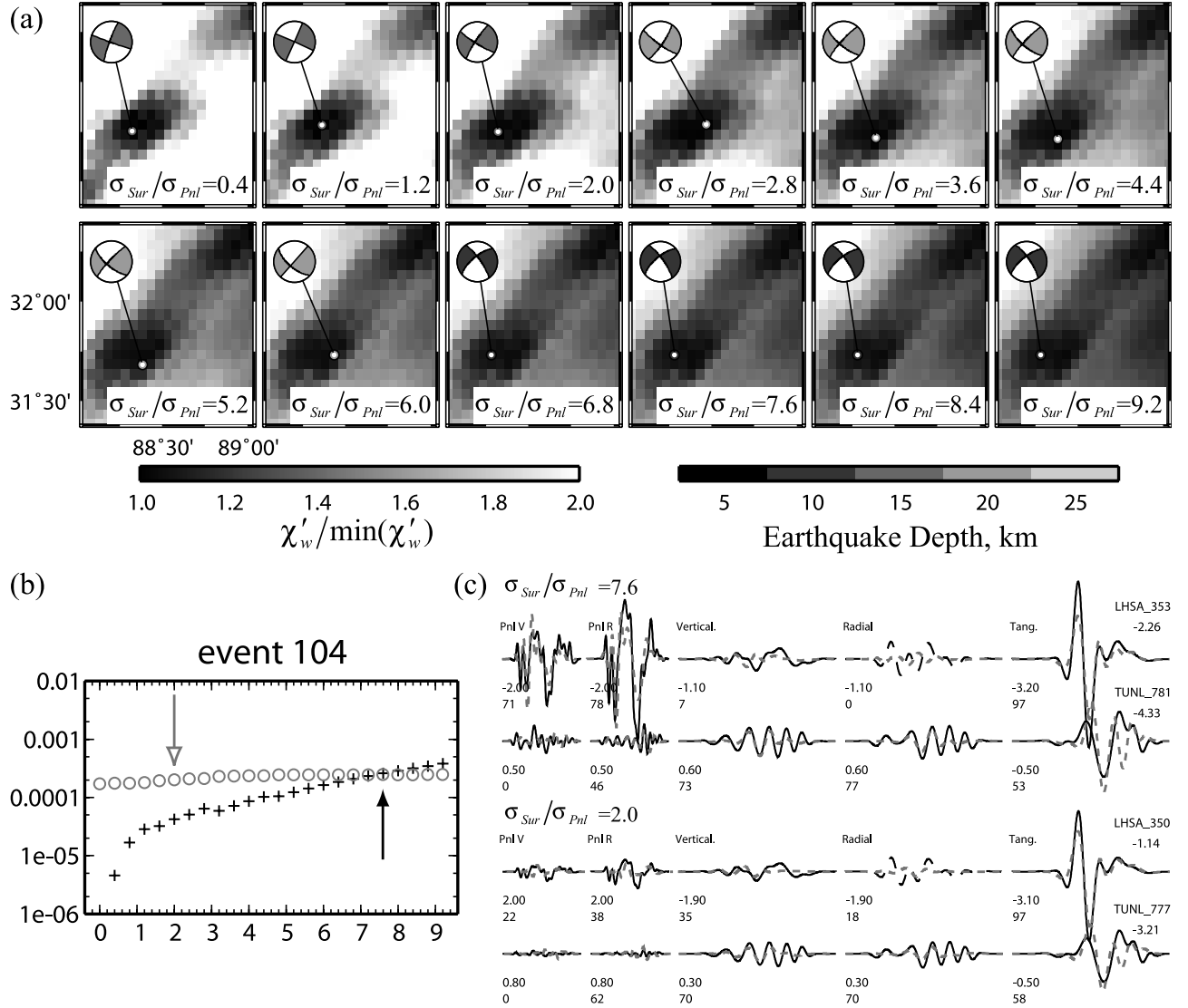


Figure 4. One-step grid search results for event 104. See Figure 3 for details.

cluster as representatives. We use the reduced chi-square χ^2/ν as shown in Figure 5 to estimate the uncertainties of the source parameters, where $\nu = \nu_{\text{Sur}} + \nu_{\text{Pnl}} - m$. The number of the unknown parameters m equals 7 in our case, since we solve for h , ϕ , δ , λ , θ , ξ and the moment magnitude M_0 [see *Bevington and Robinson, 2003*]. We choose a threshold of $\chi^2/\nu \leq 1.2$. The fact that the minimum value of χ^2/ν exceeds 1.2, such as for event 349, indicates a conflict between fitting both the waveform data and the P wave traveltimes and hence suggests an unreliable solution (denoted by “n/a” in Table 1). This is not surprising, considering the low SNR of surface waves from both stations for this event. Besides, for a few events, 325, 330a, 360, 104 and 143, a secondary solution exists (listed in Table 1), which corresponds to a local minimum of $\chi^2/\nu \leq 1.2$. The existence of a secondary solution implies a trade-off between event location and mechanism, which is mainly due to the loose constraint from noisy Rayleigh waves at both stations.

[23] In summary, the comparison between the two-station solutions from the one-step approach and the array solutions

shows remarkable consistency for both source locations and focal mechanisms. Specifically, the average offset between the two-station locations and the whole array locations is ~ 5 km.

3.3. The Two-Step Approach

[24] The above results from the one-step approach has demonstrated the ability of our new method to recover essentially the same source parameters by a distributed array using only two stations. However, this approach is a time-consuming process. It takes approximately one day on a Pentium-IV PC to find the location and focal mechanism for one event with the parameter ranges and searching steps we chose. An expedited alternative is the two-step approach, where we separate the single grid search into two, one for the source depth and mechanism, the other for the epicentral location. With the same source parameter space and the searching steps, the computation time required by the two-step approach drops by a factor of ~ 9 .

[25] We first search for an event’s depth and mechanism assuming its ISC location, where the $\delta t^{\text{Rayleigh}}$ and δt^{Love}

Table 1. Source Parameters of Depth, Mechanism, and Epicentral Location^a

ID	ISC			Array Solution by <i>Zhu et al. [2006]</i>			One-Step Approach				Two-Station Solutions				Two-Step Approach	
	Lat/Long	Δx	$h/\phi/\delta/\chi/M_w$	Lat/Long	Δx	$h/\phi/\delta/\chi/M_w$	Δx	$h/\phi/\delta/\chi/M_w$	$\sigma_{\text{Sur}}/\sigma_{\text{Pnl}}$	Δx	Lat/Long	Δx	$h/\phi/\delta/\chi/M_w$	$\sigma_{\text{Sur}}/\sigma_{\text{Pnl}}$	Δx	$h/\phi/\delta/\chi/M_w$
199	30.37/94.83	12	30.42/94.71	5/160/21/-71/4.1	30.43/94.70	2	6.1/167/20/-58/4.0	0.2	0.2	2	30.43/94.70	2	6.7/168/19/-58/4.0	0.2	2	6.7/168/19/-58/4.0
201	30.39/94.81	3	30.42/94.81	5/170/23/-63/4.0	30.44/94.78	4	6.1/180/30/-50/3.9	0.2	0.2	4	30.44/94.78	4	6.9/180/28/-50/3.9	0.2	4	6.9/180/28/-50/3.9
204	30.33/94.83	10	30.41/94.78	5/157/21/-70/4.0	30.44/94.74	5	6.9/172/21/-43/4.0	0.2	0.2	5	30.44/94.74	5	7.0/189/29/-29/4.0	0.2	5	7.0/189/29/-29/4.0
210	30.34/94.82	15	30.42/94.69	5/161/23/-71/4.0	30.44/94.70	2	5.6/180/27/-54/4.0	0.3	0.3	2	n/a	n/a	11.6/42/49/34/4.0	0.3	2	11.6/42/49/34/4.0
211	30.37/94.81	9	30.43/94.74	5/161/21/-71/3.9	30.43/94.75	1	6.5/180/26/-49/3.8	0.4	0.4	1	n/a	n/a	15/114/64/-37 ^b ; 5/29/81/-49 ^b ; 5/90/10/40 ^b ; 5/210/50/-10 ^b	0.4	1	15/114/64/-37 ^b ; 5/29/81/-49 ^b ; 5/90/10/40 ^b ; 5/210/50/-10 ^b
222	33.87/92.19	11	33.97/92.18	10/252/83/2/4.7	34.01/92.11	7	10.7/249/83/3/4.7	1.6	1.6	7	34.01/92.12	7	10.6/248/81/6/4.7	1.4	7	10.6/248/81/6/4.7
239	34.18/92.03	27	34.37/91.84	9/256/66/-8/4.1	34.36/91.83	1	10.2/252/55/-16/4.2	1.4	1.4	1	34.41/91.76	9	7.2/249/42/-18/4.2	1.6	9	7.2/249/42/-18/4.2
242	34.57/97.19	34	34.60/97.56	5/96/69/-15/4.0	34.61/97.54	3	5.3/88/52/-44/4.1	1.0	1.0	3	n/a	n/a	6.5/211/49/42/4.0	1.0	3	6.5/211/49/42/4.0
252	28.84/95.00	17	28.69/94.94	21/241/29/12/4.3	28.69/94.85	9	22.8/262/19/37/4.4	1.6	1.6	9	28.69/94.84	9	23.4/282/10/58/4.4	1.6	9	23.4/282/10/58/4.4
323	32.48/93.65	16	32.49/93.82	8/21/38/-89/4.0	32.52/93.75	7	11.5/22/41/-84/3.9	1.2	1.2	7	32.52/93.75	7	10.8/19/41/-81/3.9	1.3	7	10.8/19/41/-81/3.9
325	33.74/90.24	32	34.02/90.14	5/251/60/-16/4.5	33.97/90.22	9	7.3/84/80/6/4.4	4.0	4.0	9	33.96/90.23	11	15/62/53/19 ^b ; 5/30/50/-50 ^b	3.2	11	15/62/53/19 ^b ; 5/30/50/-50 ^b
328	34.01/88.72	21	34.04/88.94	5/221/31/-67/4.1	34.07/88.97	4	5.6/239/37/-50/4.1	1.8	1.8	4	34.07/88.97	4	8.8/75/81/-7/4.5	1.9	4	8.8/75/81/-7/4.5
329	34.01/88.81	8	34.02/88.89	5/222/33/-64/4.3	34.03/88.92	3	5.7/229/34/-61/4.2	2.8	2.8	3	n/a	n/a	6.5/238/39/-49/4.1	2.8	3	6.5/238/39/-49/4.1
330a	33.88/88.86	13	33.99/88.92	5/211/32/-72/4.2	33.98/88.94	2	6.0/229/37/-61/4.1	2.6	2.6	2	n/a	n/a	15/228/63/-28 ^b ; 5/70/50/-40 ^b ; 20/72/59/32 ^b ; 35/269/83/51 ^b ; 5/220/70/20 ^b	2.4	2	15/228/63/-28 ^b ; 5/70/50/-40 ^b ; 20/72/59/32 ^b ; 35/269/83/51 ^b ; 5/220/70/20 ^b
330b	34.09/94.26	6	34.14/94.27	11/286/63/-21/4.4	34.15/94.24	3	9.1/299/77/-19/4.5	2.2	2.2	3	34.15/94.24	3	7.2/79/70/-36/4.2	2.2	3	7.2/79/70/-36/4.2
336	32.16/94.75	20	32.10/94.56	10/43/73/-74/4.1	32.09/94.53	3	11.5/43/73/-80/4.1	1.4	1.4	3	n/a	n/a	5/240/50/-40 ^b ; 20/68/59/29 ^b ; 10/270/70/10 ^b	1.4	3	5/240/50/-40 ^b ; 20/68/59/29 ^b ; 10/270/70/10 ^b
348	33.92/88.84	13	34.04/88.83	5/212/30/-72/4.8	34.08/88.83	4	5.7/230/39/-50/4.7	4.0	4.0	4	34.08/88.83	4	7.2/89/89/-23/4.1	4.0	4	7.2/89/89/-23/4.1
349	30.03/93.88	13	30.14/93.88	8/211/69/-9/4.0	n/a	n/a	n/a	n/a	n/a	n/a	n/a	n/a	25/232/72/24 ^b ; 15/230/70/-20 ^b ; 10/90/60/20 ^b	1.2	n/a	25/232/72/24 ^b ; 15/230/70/-20 ^b ; 10/90/60/20 ^b
351	33.96/88.98	17	34.04/88.83	5/222/24/-61/4.2	34.03/88.84	2	6.5/239/28/-42/4.2	3.2	3.2	2	n/a	n/a	8.5/299/78/-19/4.5	3.2	2	8.5/299/78/-19/4.5
360	30.96/99.60	11	30.92/99.50	10/300/78/8/4.1	30.93/99.42	8	7.3/82/53/-83/4.1	2.8	2.8	8	30.93/99.42	8	13.7/263/69/56/4.1	2.0	8	13.7/263/69/56/4.1
365	30.81/99.57	15	30.91/99.67	12/294/67/-2/4.2	30.88/99.67	4	11.0/3/7/15/4.2	2.8	2.8	4	n/a	n/a	6.2/228/39/-48/4.7	1.9	4	6.2/228/39/-48/4.7
													15/69/75/-24 ^b ; 20/70/58/27 ^b ; 15/250/70/20 ^b	4.0		15/69/75/-24 ^b ; 20/70/58/27 ^b ; 15/250/70/20 ^b
													6.4/38/72/18/4.1	1.2		6.4/38/72/18/4.1
													5/220/60/20 ^b	1.2		5/220/60/20 ^b
													8.7/224/50/-18/4.2	3.2		8.7/224/50/-18/4.2
													5/239/28/-43 ^b ; 20/79/47/35 ^b ; 10/40/50/-10 ^b	3.2		5/239/28/-43 ^b ; 20/79/47/35 ^b ; 10/40/50/-10 ^b
													20.4/240/89/-32/4.1	2.0		20.4/240/89/-32/4.1
													16.1/70/74/37/4.2	1.9		16.1/70/74/37/4.2

Table 1. (continued)

ID	ISC			Array Solution by <i>Zhu et al.</i> [2006]			Two-Station Solutions										
	Lat/Long		Δx	Lat/Long			$h/\phi/\delta/\chi/M_w$			One-Step Approach				Two-Step Approach			
										Lat/Long	Δx	$h/\phi/\delta/\chi/M_w$	$\sigma_{\text{Sur}}/\sigma_{\text{PH}}$	Lat/Long	Δx	$h/\phi/\delta/\chi/M_w$	$\sigma_{\text{Sur}}/\sigma_{\text{PH}}$
002	33.94/88.85	19		34.09/88.76	5/221/30/-56/4.4		34.10/88.80	4	6.4/236/41/-39/4.3	2.4	34.09/88.80	4	7.0/227/36/-44/4.3 10/232/53/-7 ^b ; 20/75/52/13 ^b ; 5/10/60/-90 ^b ; 10/70/60/-20 ^b	2.4			
023	34.55/93.16	6		34.52/93.21	5/280/67/43/4.2		34.48/93.33	12	5.7/270/79/42/4.3	0.8	34.59/93.03	19	0.0/89/83/-10/4.1 5/109/31/41 ^b ; 5/280/70/50 ^b 11.0/79/52/53/4.3	0.7			
076	34.30/86.27	23		34.50/86.33	9/63/68/-29/4.2		34.51/86.31	2	10.8/69/72/-33/4.3	4.4	n/a		10/70/70/-40 ^b ; 10/260/70/10 ^b ; 10/230/40/-50 ^b ; 15/340/70/30 ^b ; 15/320/50/-50 ^b	4.4			
104	31.95/88.31	24		31.75/88.22	5/227/49/-23/4.5		31.73/88.28 31.74/88.43 ^b	6	8.2/230/70/-13/4.5 20.1/222/87/24 ^b	7.6	31.75/88.27	4	7.1/223/48/-30/4.4 20/229/79/27 ^b ; 5/60/60/-10 ^b ; 5/360/50/-80 ^b	6.8			
109	36.09/92.56	18		36.07/92.76	5/92/60/7/4.3		36.10/92.75	4	6.0/93/56/22/4.3	2.0	n/a		6.7/253/70/-9/4.3 5/80/60/10 ^b	1.8			
143	30.72/99.63	20		30.89/99.70	5/299/44/-52/4.0		30.89/99.69 30.94/99.60 ^b	1	7.0/301/34/-53/4.0 12.1/8/42/78 ^b	1.8	n/a		20.3/33/82/-5/4.2	1.2			
155	33.90/88.91	7		33.96/88.94	8/30/48/-79/4.2		33.94/89.02	8	11.2/27/39/-77/4.1	1.8	n/a		11.0/84/58/25/4.1 5/79/68/-40 ^b ; 5/260/50/-20 ^b ; 20/270/80/30 ^b	1.8			

^aThe Δx are the epicentral offsets in km with respect to the array locations. The unreliable solutions are denoted as "n/a."^bSmallest local minima up to five.

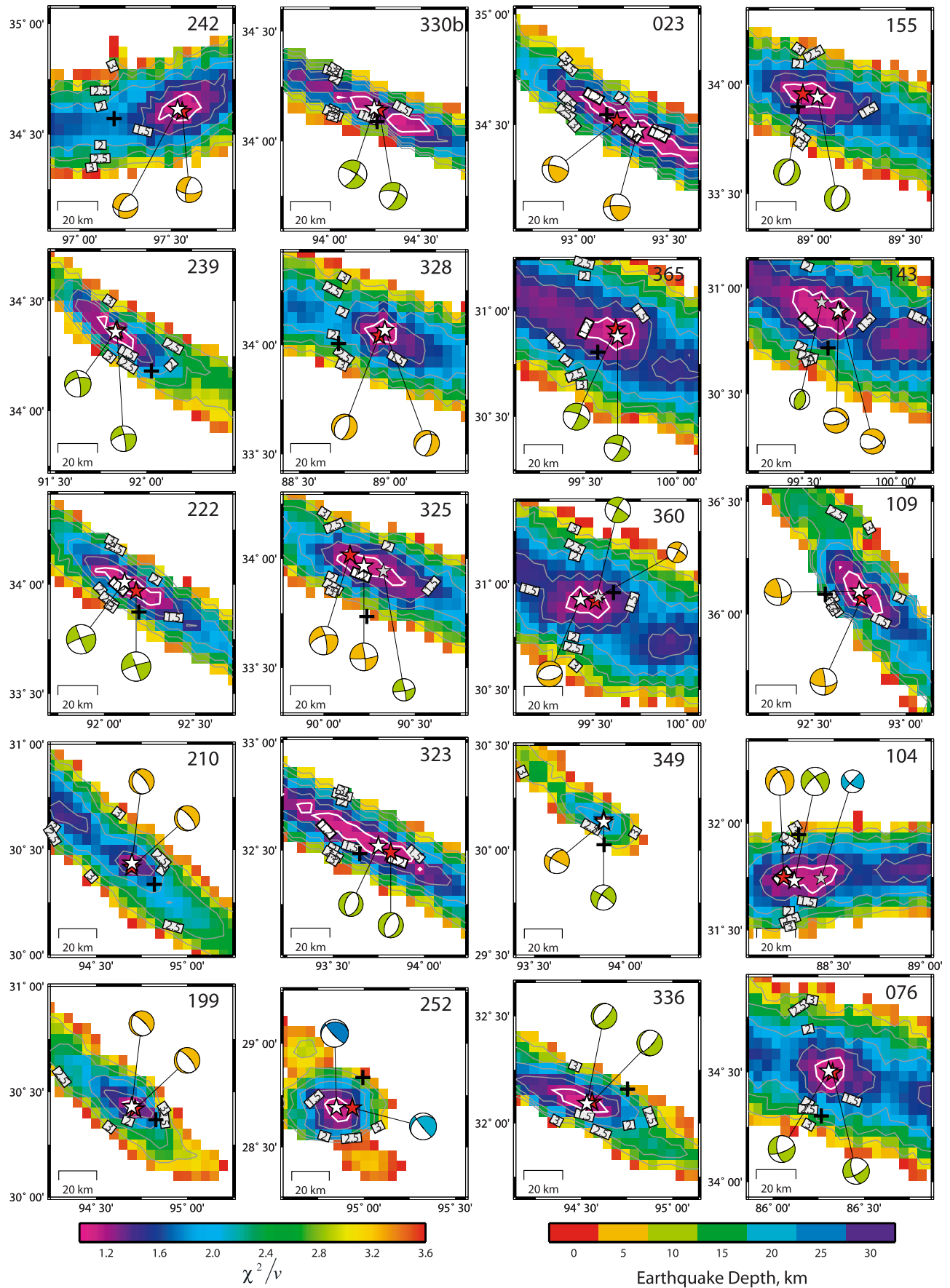


Figure 5

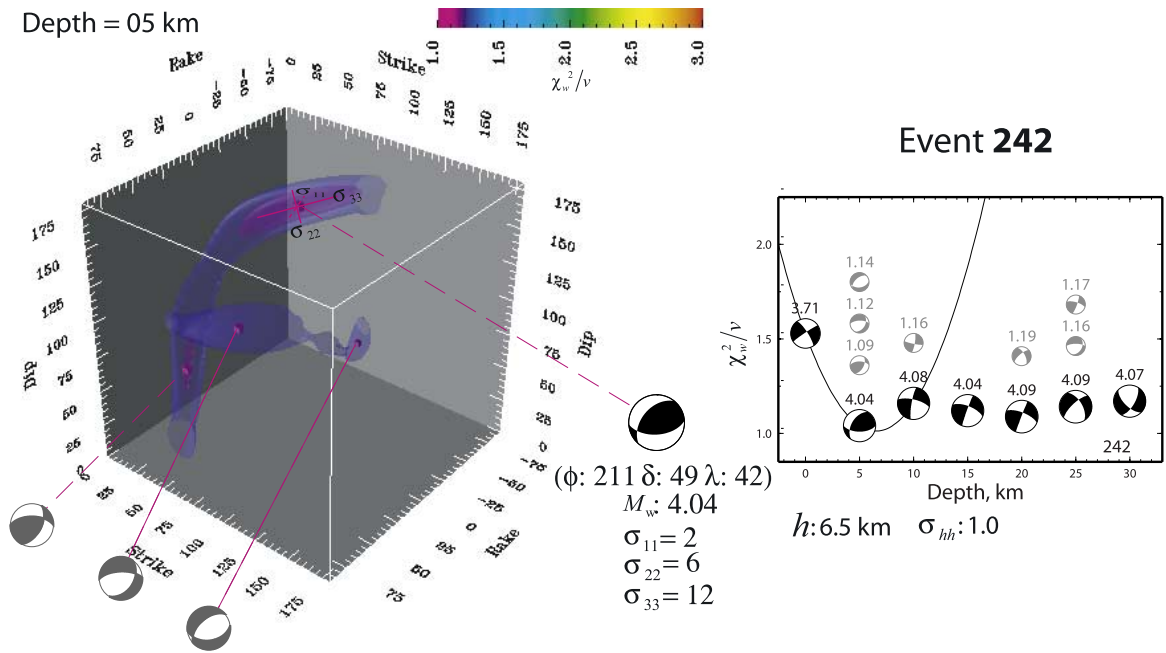


Figure 6. Resolutions of the depth and focal mechanism for event 242. (left) Reduced chi-square χ_w^2/ν in the fault parameter space for the best source depth of 5 km. Two iso- χ_w^2/ν surfaces of 1.1 and 1.2 are displayed together with the best focal mechanism (black beach ball) and local minima (gray beach balls). The uncertainties associated with the best solution can be quantified by the principal axis lengths (σ_{11} , σ_{22} and σ_{33}) of the ellipsoid that best fits the shape of the 1.2 isosurfaces at the minimum. (right) The χ_w^2/ν as a function of source depth. At each depth, besides the best solution, local minima of different mechanisms are also shown as gray beach balls with the corresponding χ_w^2/ν values displayed at the top.

are set as free parameters to account for the location error and the structural effect. We follow the similar procedure as in the one-step approach to achieve the best relative weight between PnI and surface waves. The obtained best $\sigma_{Sur}/\sigma_{PnI}$ ratios are close to their counterparts from the one-step approach (see Table 1). However, discrepancies are revealed when we compare the depth and mechanism solutions with those determined by the whole array in Table 1. Besides, quite a few events have local minima with $\chi_w^2/\nu \leq 1.2$, as shown in Figure 6 for event 242. These local minima are given in Table 1. Existence of these local minima is mainly due to cycle skipping of the surface waves. However, a large number of them would indicate a poorly constrained solution, which could be caused by low SNR of the waveform data, inappropriate velocity model, or large event location error. It is worth mentioning that the three events, 242, 328 and 076, that appear to have the most number of local minima (>5 , see Table 1) also have the largest errors in their ISC locations with respect to their relocations by *Zhu et al.* [2006]. In fact, if we simply discard these solutions with a large number of local minima, the two-station solutions basically agree with the array

solutions, even though they systematically have larger uncertainties.

[26] We then take the obtained source depths and mechanisms to relocate the events, where the surface wave segments are not allowed to float. The relocation results are summarized in Table 1, and Figure 7 displays the details for the same 20 events shown in Figure 5. Quite a few events in Figure 7, such as 210, 242, 336, 360, 365, 076, 109, 143 and 155 show a minimal χ^2/ν value exceeding 1.2, which indicates the relocations with the assumed depth and mechanism fail to explain the travel times of P and surface waves. The discrepancies are due to the phase shifts of the synthetic surface waves from the fixed source depth and mechanism. Therefore we mark such relocations as unreliable (denoted “n/a” in Table 1). Correspondingly, the adopted source depths and mechanisms are also questionable.

[27] It appears in Figure 7 that for the relocations we trust ($\chi^2/\nu \leq 1.2$), their offsets with respect to the array locations are generally less than 10 km. Moreover, the adopted source depths and mechanisms also agree well with the array solutions. Trade-offs between source depth, mechanism, and epicenter location are rarely observed, except for events

Figure 5. Results of the one-step approach for 20 events. Contours show the reduced chi-square χ^2/ν values with the 1.2 contour in white. For each event, the epicenter that corresponds to the min (χ^2/ν) is indicated by the white star, together with the obtained focal mechanism. The depth of the event is indicated by the color of the “beach ball.” In the case of existence of a secondary solution, it is denoted by a smaller gray star, as shown for events 325, 360, 104, and 143. Also shown for comparison are the events’ ISC locations (black crosses) and the array determined solutions (red stars) by *Zhu et al.* [2006].

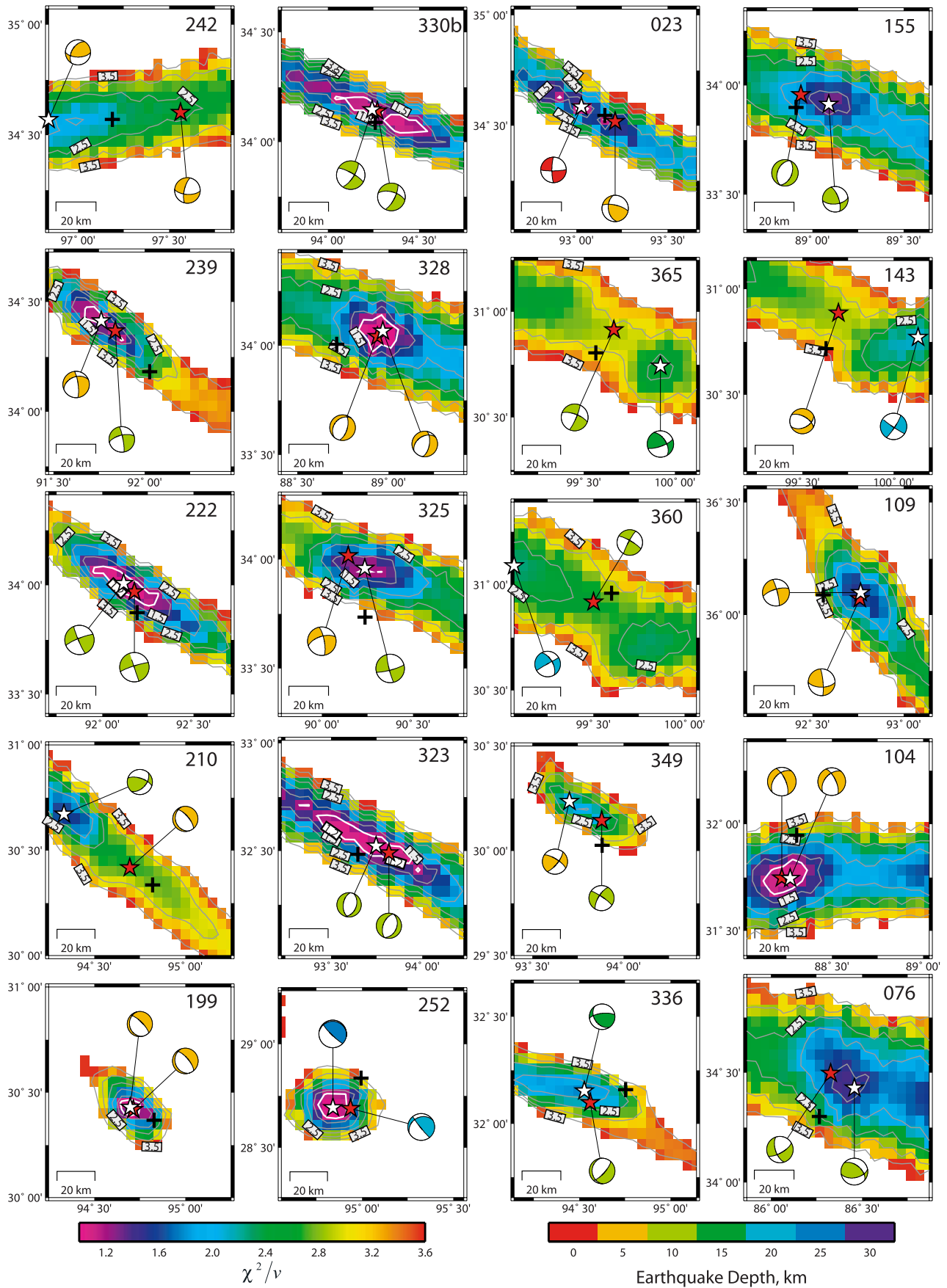


Figure 7. Results from the two-step approach for the same 20 events in Figure 5. See Figure 5 for details.

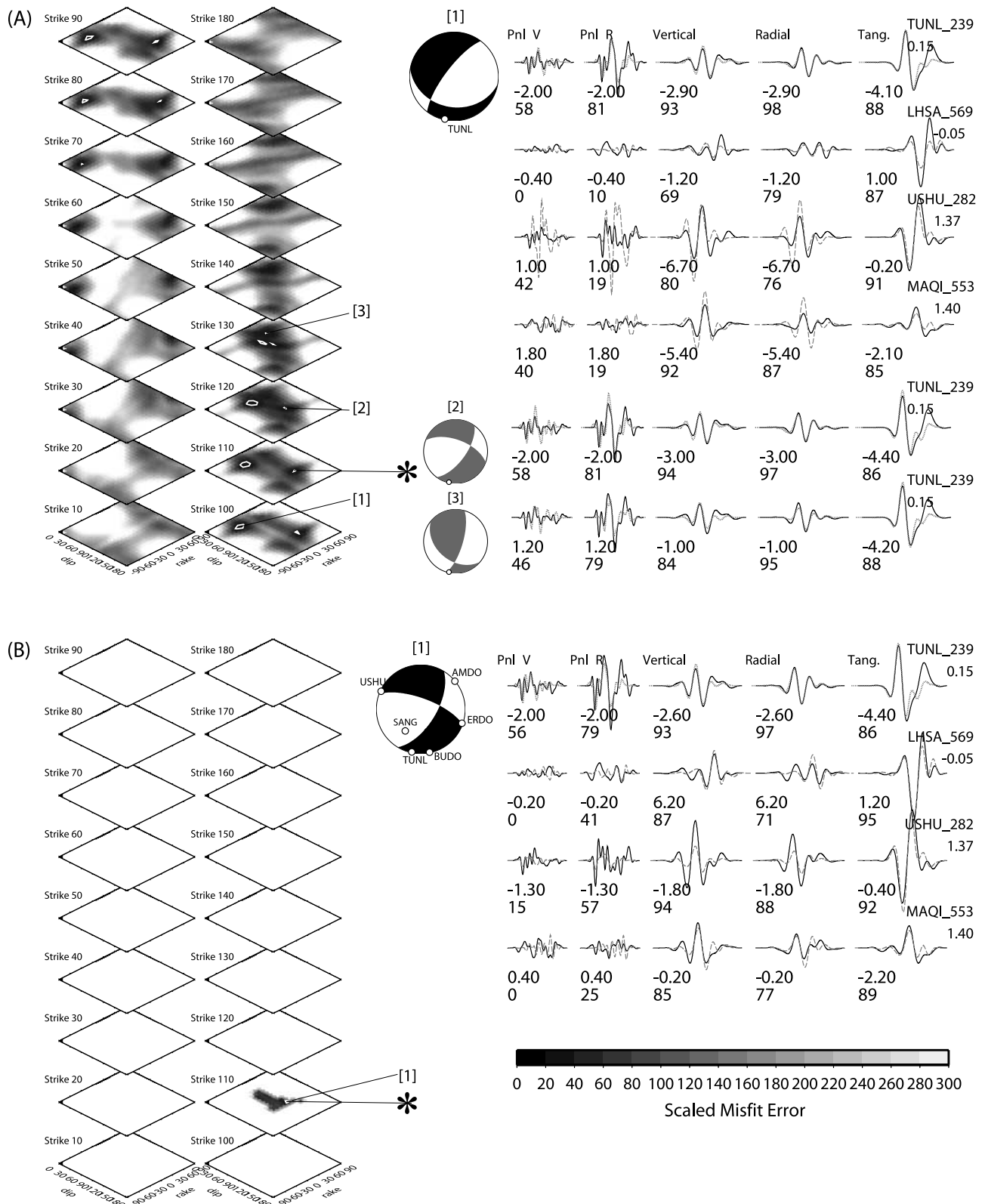


Figure 8. The focal mechanism solution using (a) station TUNL only, and (b) station TUNL plus first-motion polarities from additional stations, USHU, AMDO, ERDO, BUDO, and SANG. A $\sigma_{\text{Sur}}/\sigma_{\text{PnI}}$ ratio of 2.2 is used. The waveform misfit errors normalized by the minimum value are shown in the left. The best solution is denoted by [1] and local minima as [2] and [3]. The asterisk indicates the array determined solution. The corresponding waveform fits are shown in the right, together with the predictions for the three stations: LHSA, USHU, and MAQL.

239, 252, 325, and 023. However, the offset between an unreliable relocation and the array location generally exceeds 20 km, and the assumed source depth and mechanism also differ from the array solution. So, the two-step approach does not always give the correct solution, but the reliability of a solution can be evaluated by the reduced chi-square value. Also note the uncertainties of the relocations (the 1.2 contour) are systematically underestimated, since the correlation of the epicenter location with the source depth and mechanism has not been taken into account. If we discard the unreliable relocations, the two-step approach actually improves the locations of 15 events with an average mislocation error reduction from ~ 16 km in their initial ISC locations to ~ 7 km.

4. Discussion and Conclusions

[28] In this paper, we developed a new technique CAPloc to simultaneously determine source mechanism and location of a small regional event using complete three-component seismograms. A similar effort was attempted by *Tajima et al.* [2002] using long-period whole waveforms (20–50 mHz). Our method is superior in that both *Pnl* and surface waves are modeled to provide better constraints on source depth and orientation. Moreover, fitting differential travel times between the *P* and surface waves helps eliminate the influence of a wrong event origin time. To take full advantage of both *Pnl* and surface waves, we introduced an adaptive weighting scheme. The relative weight between *Pnl* and surface waves is derived from the variances of their waveform residues to balance their contributions. An appropriate weight of *Pnl* to surface waves is important, especially when few stations are available. We tested two approaches of CAPloc. They are essentially the same, in that the entire records are modeled with the separations between the *P* and surface waves adjusted from known calibration information. However, the two-step approach, though requires much less computer time, is vulnerable in determining the source depth and mechanism using only two stations. The one-step approach better accounts for the trade-offs between an event location and mechanism; hence it gives better result.

[29] The empirical-path-specific corrections (EPSCs) are essential to the success of the method, and their uncertainties directly affect the uncertainty of the source location. Since an event location is mainly constrained by the differential travel times between the *P* and surface waves, a 0.5 s uncertainty in the EPSCs would be mapped into an uncertainty of ~ 3 km in the events' epicentral distances. For the optimal case where the two stations differ in azimuth by $\sim 90^\circ$, the event location could be well constrained within a radius of ~ 3 km. Otherwise the uncertainty range of the epicenter location tends to be elongated, suggesting poor constraint in a certain direction as we have seen in both Figures 5 and 7. Note the relatively large uncertainties of the epicenter locations are due to the discrete Green's functions with a distance interval of 5 km. Since we use the closest Green's function for each station, a 2.5 km error in the epicentral distance could result. This suggests a denser Green's function library should be used, or the distance error of the Green's functions be corrected to achieve better location precision.

[30] We assume a fixed 0.5 s uncertainty in the EPSCs. However, considering their possible variations over the spatial parameter space, especially the 3-D hypocenter space in the one-step approach, the 0.5 s uncertainty may represent a lower bound. Moreover, the uncertainties of the EPSCs might vary for different paths, depending on the goodness of the velocity model and how well the events for the calibration purpose are determined. A high resolution tomographic map will enable timely EPSC predictions plus better controlled uncertainty estimates, which will be pursued in a future effort.

[31] We restrict ourselves to using data from only two stations to demonstrate that the complete three-component seismograms from as few as two stations suffice in determining both location and mechanism of a regional event. However, additional arrival time or first-motion polarity data of short-period stations, if available, can be incorporated easily into the approach. Adding arrival times can help constrain the event location. Also, polarities could be quite useful in narrowing the uncertainties of a focal mechanism solution, even if waveform data from only one station are available. Figure 8 gives such an example for event 330b, where we use station TUNL alone to retrieve the source depth and orientation. We obtain a well-defined depth of 9.6 km, which agrees with the two station as well as the array solutions. However, the focal mechanism is poorly constrained (Figure 8a). Figure 8b shows the remarkable improvement by adding the polarities from some other stations, where the first *P* wave motion is easily discernible. Similar results are obtained when we use another station or another event.

[32] In summary, this study addresses the issue of modeling small regional events that are poorly monitored. A magnitude threshold of ~ 3.5 is anticipated for the frequency band we currently use. We demonstrate that regional seismograms from as few as two stations suffice to determine both source location and mechanism provided that we have path calibration information. For the tested 28 events, the two-station solutions agree well with those determined from the whole PASSCAL array. In particular, we improve the events' ISC locations with an average mislocation error reduction from ~ 16 km to ~ 5 km.

[33] **Acknowledgments.** The authors are grateful to Dave Wald and Arthur Rodgers, whose comments have helped to improve the manuscript. This work was supported by NSF grant EAR-0337491. L.Z. was partially supported by USGS NEHRP grant 03HQGR0100. California Institute of Technology Seismological Laboratory contribution 9126.

References

- Bevington, P. R., and D. K. Robinson (2003), *Data Reduction and Error Analysis*, McGraw-Hill, New York.
- Bondár, I., and R. G. North (1999), Development of calibration techniques for the comprehensive nuclear-test-ban treaty (CTBT) international monitoring system, *Phys. Earth Planet. Inter.*, 113, 11–24.
- Bondár, I., R. G. North, and G. Beall (1999), Teleseismic slowness-azimuth station corrections for the international monitoring system seismic network, *Bull. Seismol. Soc. Am.*, 89(4), 989–1003.
- Dreger, D., and D. V. Helmberger (1993), Determination of source parameters at regional distances with three-component sparse network data, *J. Geophys. Res.*, 98(B5), 8107–8125.
- Fan, G., and T. Wallace (1991), The determination of source parameters for small earthquakes from a single, very broadband seismic station, *Geophys. Res. Lett.*, 18(8), 1385–1388.
- Hauksson, E. (2001), Southern California seismic network: Caltech/USGS element of TriNet 1997–2001, *Seismol. Res. Lett.*, 72, 697–711.

- Helmberger, D. V. (1983), Theory and application of synthetic seismograms, in *Earthquakes: Observation, Theory and Interpretation*, pp. 174–222, Soc. Ital. di Fisi., Bologna.
- Kennett, B. L. N., and F. Ringdal (2001), Locating seismic events in the CTBT context, *Pure Appl. Geophys.*, *158*, 7–18.
- Kremenetskaya, E., V. Asming, and F. Ringdal (2001), Seismic location calibration of the European Arctic, *Pure Appl. Geophys.*, *158*, 117–128.
- Langin, W. R., L. D. Brown, and E. A. Sandvol (2003), Seismicity of central Tibet from project INDEPTH III seismic recordings, *Bull. Seismol. Soc. Am.*, *93*, 2146–2159, doi:10.1785/0120030004.
- Langston, C. A. (1981), Source inversion of seismic waveforms: The Koyna, India, earthquakes of 13 September 1967, *Bull. Seismol. Soc. Am.*, *71*, 1–24.
- Leitner, B., D. Eberhart-Phillips, H. Anderson, and J. L. Náblek (2001), A focused look at the Alpine fault, New Zealand: Seismicity, focal mechanisms, and stress observations, *J. Geophys. Res.*, *106*(B2), 2193–2220.
- Okada, Y., K. Kasahara, S. Hori, K. Obara, S. Sekiguchi, H. Fujiwara, and A. Yamamoto (2004), Recent progress of seismic observation networks in Japan – Hi-net, F-net, K-net and KiK-net, *Earth Planets Space*, *56*(8), xv–xxviii.
- Owens, T. J., G. E. Randall, F. T. Wu, and R. S. Zeng (1993), PASSCAL instrument performance during the Tibetan plateau passive seismic experiment, *Bull. Seismol. Soc. Am.*, *83*, 1959–1970.
- Ritsema, J., and T. Lay (1993), Rapid source mechanism determination of large ($M_w \geq 5$) earthquakes in the western United States, *Geophys. Res. Lett.*, *20*(15), 1611–1614.
- Romanowicz, B., D. S. Dreger, M. Pasyanos, and R. Uhrhammer (1993), Monitoring of strain release in central and northern California, *Geophys. Res. Lett.*, *20*(15), 1643–1646.
- Ryaboy, V., D. R. Baumgardt, P. Firbas, and A. M. Dainty (2001), Application of 3-D crustal and upper mantle velocity model of North America for location of regional seismic events, *Pure Appl. Geophys.*, *158*, 79–103.
- Stevens, J. L., D. A. Adams, and G. E. Baker (2001), Improved surface wave detection and measurement using phase-matched filtering with a global one-degree dispersion model, paper presented at the 23rd Seismic Research Review: Worldwide Monitoring of Nuclear Explosions, Jackson Hole, Wyo., 2–5 Oct.
- Tajima, F., C. Megnin, D. S. Dreger, and B. Romanowicz (2002), Feasibility of real-time broadband waveform inversion for simultaneous moment tensor and centroid location determination, *Bull. Seismol. Soc. Am.*, *92*(2), 739–750.
- Teng, T., L. Wu, T. Shin, Y. Tsai, and W. H. K. Lee (1997), One minute after: Strong-motion map, effective epicenter, and effective magnitude, *Bull. Seismol. Soc. Am.*, *87*, 1209–1219.
- Thio, H.-K., and H. Kanamori (1995), Moment-tensor inversions for local earthquakes using surface waves recorded at TERRAScope, *Bull. Seismol. Soc. Am.*, *85*, 1021–1038.
- Uhrhammer, R., D. S. Dreger, and B. Romanowicz (2001), Best practice in earthquake location using broadband three-component seismic waveform data, *Pure Appl. Geophys.*, *158*, 259–276.
- Yacoub, N. K. (1996), Maximum spectral energy arrival time for epicenter estimation. Part I: Rayleigh waves, *Seismol. Res. Lett.*, *67*(2), 62.
- Yang, X., I. Bondár, K. McLaughlin, R. North, and W. Nagy (2001a), Path-dependent regional phase travel-time corrections for the International Monitoring System in North America, *Bull. Seismol. Soc. Am.*, *91*, 1831–1850.
- Yang, X., I. Bondár, K. McLaughlin, R. North, and W. Nagy (2001b), Source specific station corrections for regional phases at Fennoscandian stations, *Pure Appl. Geophys.*, *168*, 35–57.
- Zhao, L. S., and D. V. Helmberger (1994), Source estimation from broadband regional seismograms, *Bull. Seismol. Soc. Am.*, *84*, 91–104.
- Zhu, L., and D. V. Helmberger (1996), Advancement in source estimation techniques using broadband regional seismograms, *Bull. Seismol. Soc. Am.*, *86*, 1634–1641.
- Zhu, L., and L. A. Rivera (2002), A note on the dynamic and static displacements from a point source in multi-layered media, *Geophys. J. Int.*, *148*, 619–627.
- Zhu, L., Y. Tan, D. V. Helmberger, and C. K. Saikia (2006), Calibration of the Tibetan plateau using regional seismic waveforms, *Pure Appl. Geophys.*, in press.

D. V. Helmberger and Y. Tan, Seismological Laboratory, California Institute of Technology, Pasadena, CA 91125, USA. (ytan@gps.caltech.edu)

C. K. Saikia, URS Co., 566 El Dorado Street, 2nd Floor, Pasadena, CA 91101-2560, USA.

L. Zhu, Department of Earth and Atmospheric Sciences, Saint Louis University, St. Louis, MO 63103, USA.